The role of three-dimensional morphology on the efficiency of hybrid polymer solar cells

Stefan D. Oosterhout[1], Martijn M. Wienk[1], Svetlana S. van Bavel[2,3], Ralf Thiedmann[4], L. Jan Anton Koster[1], Jan Gilot[1], Joachim Loos[2], Volker Schmidt[4] and René A. J. Janssen[1*]

---

[1] Molecular Materials and Nanosystems, Eindhoven University of Technology, PO Box 513, 5600 MB Eindhoven, The Netherlands.

[2] Laboratory of Materials and Interface Chemistry and Soft Matter Cryo-TEM Research Unit, Eindhoven University of Technology, P.O. Box 513, 5600 MB Eindhoven, The Netherlands.

[3] Dutch Polymer Institute P.O. Box 902, 5600 AX Eindhoven, The Netherlands.

[4] Institute for Stochastics, Ulm University, 89069 Ulm, Germany.

[*] e-mail: r.a.j.janssen@tue.nl

Abstract: The efficiency of polymer solar cells critically depends on the intimacy of mixing of the donor and acceptor semiconductors used in these devices to create charges and on the presence of unhindered percolation pathways in the individual components to transport holes and electrons. The visualisation of these bulk heterojunction morphologies in three dimensions has been challenging and has hampered progress in this area. Here, we spatially resolve the morphology of 2% efficient hybrid solar cells consisting of poly(3-hexylthiophene) (P3HT) as donor and ZnO as acceptor in the nanometre range by electron tomography. The morphology is statistically analyzed for spherical contact distance and percolation pathways. Together with solving the three-dimensional exciton diffusion equation, a consistent and quantitative correlation between solar cell performance, photophysical data and the three-dimensional morphology has been obtained for devices with different layer thickness that enables differentiating between generation and transport as limiting factors to performance.

Efficient organic solar cells utilize a bulk heterojunction of two semiconductors with off set energy levels to create charges. By intimately mixing electron donor and acceptor materials the intrinsic limitations related to the low mobility and lifetime of excitons in organic semiconductors can be overcome, resulting in effective carrier generation at the extended donor-acceptor interface. The most efficient organic solar cells combine *p*-type conjugated polymers with *n*-type fullerenes,[1] which have recently reached efficiencies of 6%.[2,3] Control over the morphology of the blend by proper choice of processing conditions is generally essential to reach this level of performance and one of the traditional challenges in the field of organic solar cells lies in optimisation of the morphology of the mixed layer. As an alternative to fully organic solar cells, hybrid solar cells use a combination of organic and inorganic materials. This concept has been demonstrated by combining semiconducting polymers as donor with different inorganic materials, including CdSe,[4,5] TiO_2[6,7] and ZnO,[8-10] as acceptor. Potential advantages of the inorganic semiconductors are a high dielectric constant which facilitates carrier generation processes, a high carrier mobility, and thermal morphological stability of the blended materials. Ultimately, hybrid cells offer the prospect of actual control over the morphology of the blend by first constructing the inorganic scaffold with the proper layout and dimensions,[11-13] but until now the best hybrid solar cells were made by simultaneous deposition of the two components. This often involves precarious processing, due to the rather different nature of the materials involved. These drawbacks can largely be circumvented by the *in-situ* generation of the inorganic semiconductor inside the organic material.[14,15] In this process a well soluble organometallic precursor is deposited from solution together with the semiconducting polymer. During and after this deposition the precursor is converted, by reacting with moisture from the surrounding atmosphere, to an inorganic network inside the polymer film. This has provided 1.4% efficient photovoltaic cells, using diethylzinc as ZnO precursor and P3HT as the semiconducting polymer.[16]

The reasons for the reduced efficiency of hybrid solar cells compared to the more efficient polymer:fullerene cells are only partly understood and need to be analyzed to further increase the performance. Here we describe and analyze *in-situ* P3HT:ZnO solar cells that reach a power conversion efficiency of 2%. Photoinduced absorption spectroscopy and three-dimensional electron microscopy of the active layers, combined with statistical analysis of percolation paths and solving the exciton diffusion equation are used to provide an unprecedented detailed insight in the role of the nanoscale morphology in creating and transporting charges in these bulk heterojunctions. Such analysis enables a unique and quantitative insight into the loss mechanisms associated with morphology that control, and ultimately limit, the power conversion of these rather efficient P3HT:ZnO hybrid solar cells.

The active layer of the photovoltaic cells was applied by spin coating a blend of diethylzinc and P3HT from a mixture of chlorobenzene, toluene and tetrahydrofuran (THF) onto a transparent electrode, consisting of poly(3,4-ethylenedioxythiophene): poly(styrenesulfonate) (PEDOT:PSS) on an indium tin oxide (ITO) covered glass substrate. During spin coating, the diethylzinc was exposed to humidity causing hydrolysis and formation of $Zn(OH)_2$. The subsequent condensation reaction is completed by annealing the film at 100 °C to form an interpenetrating network of ZnO inside the P3HT. Electron diffraction experiments evidence the presence of crystalline P3HT and ZnO domains in these active layers (see Supplementary Information). These mixed films do not visibly scatter light, indicating that no coarse phase separation between the organic and inorganic component takes place during the deposition process. An aluminium top electrode completes the device.

Several mass ratios of P3HT versus ZnO were tested. A 1:1 ratio (w/w) was found to give the best performance. This translates into a ZnO volume fraction of ca. 20% only, noticeably smaller than what is commonly used in polymer:fullerene solar cell devices, where the optimal fullerene content generally exceeds 50%. Also the thickness of the P3HT:ZnO active layer was systematically varied between 50 and 250 nm, by adjusting the spin rate during the coating process, while keeping the same P3HT and diethylzinc concentration. Despite some spread in the results, a clear trend is observed: the performance of the devices improves with increasing photoactive layer thickness, mainly as a result of increasing current densities. The overall best performance was obtained for a device with an active layer thickness of 225 nm. Under illumination with 100 mW cm^{-2} simulated solar light this device delivers an open circuit voltage (V_{OC}) of 0.75 V, a short circuit current density (J_{SC}) of 5.2 mA cm^{-2} and a fill factor (FF) of 0.52, resulting in an estimated device efficiency of 2.0%. Spectral response measurements (Fig. 1b) reveal a maximal external quantum efficiency (EQE) of 44 % at 520 nm. The broad, rather flat shape of the spectral response is related to the thickness of the device. Convolution of the EQE with the AM1.5G spectrum affords a current density of 5.6 mA cm^{-2}, which is in reasonable agreement with the value obtained from *J*-*V* measurements.

It is quite uncommon for polymer solar cells to have an optimal layer thickness significantly larger than 100 nm, because the many material combinations suffer from charge collection limitations at larger thicknesses. P3HT:PCBM is one notable exception,[17] demonstrating that in P3HT carrier mobilities are sufficiently high to allow thick photoactive layers. The good performance of the relatively thick P3HT:ZnO layer is a strong indication that electron collection through the ZnO phase occurs quite effectively as well, despite the relatively low ZnO content.

Thicker P3HT:ZnO cells outperform the thinner devices thanks to increasing current density, while the fill factor and open circuit voltage remain constant. The increase of current density with increasing layer thickness is shown in Fig. 1c. For comparison the number of photons absorbed by the P3HT:ZnO layer is included. The absorption was calculated by optical modelling, integrating over all wavelengths using the complex refractive index of the mixed layer ($\tilde{n} = n + i \cdot k$, with n the refractive index and k the extinction coefficient) as determined by ellipsometry. The modelling was performed on the entire stack of layers (glass/ITO/PEDOT:PSS/P3HT:ZnO/Al) in the device and thus accounts for interference effects (see Supplementary Information). Fig. 1c shows that the increasing current density with layer thickness is noticeably larger than the absorption increase. This can be quantified with the internal quantum efficiency (IQE), which is the ratio between the measured J_{SC} and the number of absorbed AM1.5 photons per unit area and time. The IQE (Fig. 1d) increases significantly with layer thickness from 20% for 50 nm thick cells up to 50% for cells with active layer thicknesses > 150 nm. Hence, in thicker layers, not only more photons are absorbed, but these photons are also more efficiently transferred into collected current. This is somewhat counterintuitive, because one would expect that charge collection becomes more difficult for thicker layers, due to the larger distances over which the carriers need to be transported and the smaller electric field over the layer.

To further investigate the observed IQE differences, photoinduced absorption (PIA) measurements were carried out on three P3HT:ZnO photovoltaic cells with different layer thickness (44, 54 nm and 151 nm). For all three samples excitation at 488 nm (2.54 eV) results in photoinduced bleaching bands of neutral P3HT at 1.9 eV, 2.2 eV, and 2.35 eV (Fig. 2, normalized at the bleaching signal at 2.2 eV to correct for differences in layer thickness). Moreover, the characteristic absorption bands of the polymer radical cation at 0.5 and 1.3 eV are observed, unambiguously demonstrating photoinduced charge generation in this blend.[18] The low-energy absorption at 0.5 eV is relatively large because at this energy also electrons injected into the ZnO contribute to the PIA signal.[8,19] The spectra also exhibit a peak at 1.06 eV, which is related to a P3HT triplet state.[18] This indicates that quenching of the initially formed singlet exciton is not quantitative, leaving enough time for intersystem crossing to the triplet state for a significant fraction of the excitations. Without knowing the exact absorption coefficient and lifetime of the different photoinduced states one cannot quantitatively assess their yields, but comparing the ratio between polaron and triplet bands does provide relevant information about the relative yields. For thicker layers the radical cation bands increase significantly compared to the triplet absorption, suggesting a higher carrier generation efficiency, in accordance with the observed higher IQE for thicker layers. Photoluminescence (PL) spectroscopy on P3HT:ZnO films confirmed the incomplete exciton quenching. Quantitatively analysis was severely hampered by the intrinsic low PL efficiency in P3HT,[20] which is mainly determined by disordered regions and generally not representative for the majority of excitons.[20,21]

The observed incomplete charge generation in hybrid polymer:ZnO films makes them distinctly different from photoactive blends with fullerenes as electron acceptor, where exciton quenching is generally quantitative, even at very low fullerene contents. This could be related to a higher miscibility for the molecular acceptors with the donor polymer, affording better dispersion of the acceptor (domains) inside the polymer matrix.[22,23]

A sub optimal morphology is one possible cause for incomplete charge carrier generation, demonstrated by PIA measurements. To examine the morphology of the P3HT:ZnO film, transmission electron microscopy (TEM) was used. The bright-field

TEM image of a cross section of a typical complete device (Fig. 3a) shows that the photoactive layer is much rougher than all layers underneath. In the image ZnO shows up as the darker regions as a consequence of a higher electron density. Evidently, ZnO is not homogenously dispersed inside the polymer matrix, especially at the interface with the PEDOT:PSS a layer of pure P3HT is present. This layer is at least 10 nm thick causing excitons generated within the first few nanometres from the PEDOT:PSS interface not to reach a ZnO interface to create charges. Possibly, (part of) the triplets observed with PIA originate from this layer. This interface layer constitutes a larger fraction for thinner devices, which could explain the larger triplet signals in these samples. In absolute terms, however, the number of excitons that are expected to be lost in this P3HT interface layer is not large enough to completely account for the measured IQE losses, which exceed 50% for all devices.

More detailed TEM analyses were carried out on freestanding films. Representative mixed films of different thicknesses (57, 100, and 167 nm) were spin coated on PEDOT:PSS and then floated on water, leaving P3HT:ZnO films that were analysed by electron tomography.[24] The snapshots of the reconstructed volume of these films are shown in Fig. 3b. A threshold was applied to the raw data as obtained by electron tomography in such a way that ZnO appears yellow and P3HT looks transparent. Ostensibly a large difference between the three films is obtained, displaying finer phase separated domains with increasing layer thickness. Especially, the thinnest film displays much larger domains, both for the ZnO and the P3HT. The presence of P3HT domains which are substantially larger than the exciton diffusion lengths in P3HT is consistent with the large triplet signals in PIA measurements and the low IQE in the thin devices.

In order to quantify the relevant morphological parameters, an extensive statistical analysis of the 3D-TEM images was performed. Therefore, the original 3D-TEM data of the bulk of the film (ca. 60% of the total thickness) were binarized to decide which voxels (3-D data points) are ZnO and which are P3HT. The results are summarized in Table 1.

In the two thickest layers the estimated ZnO volume fraction is close to the expected value of 19%, based on the ratio of diethylzinc and P3HT in the spin coating solution. The ZnO content in the thinnest layer is significantly lower at 13%. This is tentatively rationalized by a comparatively large fraction of the diethylzinc evaporating during spin coating with the higher spin rate applied for this thin layer. The low ZnO content of the thinnest film partially accounts for the relatively large observed P3HT domains.

Next, spherical contact distances, defined as the distance from a certain voxel of one material to the nearest voxel of the other material, were determined for these three films. Because under operation, excitons are primarily generated inside P3HT, we focus on the distance distribution from P3HT to ZnO. Fig. 4a shows the probability to find P3HT at a certain shortest distance to a ZnO domain. For the 100 and 167 nm thick films, most P3HT lies well within a shortest distance of 10 nm from ZnO. On the other hand, the 57 nm thick sample displays a large amount of polymer at shortest distances as high as 25 nm from an interface with ZnO. This analysis substantiates that coarser phase separation is present in thinner layers.

It is not exactly clear what governs the large morphology differences. During deposition several processes take place simultaneously: evaporation of three different solvents and diethylzinc, adsorption of water, reaction of diethylzinc with water, evaporation of condensation reaction products, gelation and/or precipitation of P3HT and the inorganic material. The relative rate of these processes will determine the final morphology. Our results suggest that these relative rates change significantly with increasing spin rate during deposition. Attempts to further improve the morphology of the thin layers by changing processing conditions (solvents, concentration, spin rate) have so far been unsuccessful.

To quantify the effect of the coarseness of the phase separation on the charge carrier generation exciton diffusion in the active layer has been modelled. The diffusion of excitons in the polymer phase can be described by the diffusion equation

$$\frac{\mathrm{d}n}{\mathrm{d}t} = -\frac{n}{\tau} + D\nabla^2 n + g, \tag{1}$$

where D is the diffusion constant, n is the exciton density, τ is the exciton lifetime, and g is the rate of exciton generation. The exciton lifetime and exciton diffusion rate in P3HT are taken from the literature: $\tau = 400$ ps and $D = 1.8 \times 10^{-7}$ m^2 s^{-1}.[25] It is assumed that at an interface with ZnO excitons are efficiently quenched,[9] i.e. $n = 0$. This assumption causes the calculated quenching to be an upper limit to actual charge generation efficiency. In this respect we note that exciton quenching at the P3HT/ZnO interface has recently been questioned,[26] but we stress that the alternative explanation, *i.e.* that free charges are directly generated in P3HT with a quantum yield of 1.7% and ZnO only acts to collect the electrons,[26] is not compatible with the IQE ≈ 50% observed here. Figures 5a-c show the calculated exciton quenching efficiency η_Q for different layer thicknesses in bulk material obtained by solving the diffusion equation using cyclic boundary conditions and reveal that exciton quenching is far more efficient in the thicker layers as a consequence of their finer morphology.

However, with active layers as thin as 60 nm, the effect of the electrodes cannot be ignored. It is well established that excitons in conjugated polymers can be quenched at both PEDOT:PSS and LiF/Al electrodes.[27-29] The quenching is associated with long-range energy transfer of excitons to the electrode interface assisted by exciton diffusion. Exciton quenching at the electrodes will not contribute to the photocurrent generation. To emulate the effect of electrodes two perfectly quenching planes were used as boundary conditions, instead of imposing cyclic boundary conditions. The effect of introducing electrodes is especially striking for the thinnest layer (Table 1): 32% of excitons are quenched by the electrodes and do not contribute to the current. The presence of electrodes also impacts on the efficiency of quenching by ZnO: as a sizeable fraction of excitons diffuses towards the electrodes, fewer excitons will be quenched by ZnO and contribute to the photocurrent. For the thicker layers (100 nm and 167 nm) these effects are far less pronounced. This is in part due to the much finer morphology and in part due the larger layer thickness, as both these factors result in most excitons being generated closer to ZnO than to an electrode. Figures 5d-f display vertical cross sections of the quenching efficiency in the presence of the electrode.

Besides charge carrier generation, also carrier collection is essential for solar cell operation. Efficient collection relies on continuous pathways for both carriers. In view of the large volume excess of polymer in the blend, connectivity of this material will not be a limiting factor. The fraction of ZnO voxels that is interconnected via other ZnO voxels to the top of the investigated slab is quite high, at values well over 90% for all three layers, despite the low ZnO content (Table 1). The connectivity is smaller for thicker layers, likely because larger distances have to be crossed. However, mere continuity may not be enough to effectively collect the charges. Within a continuous phase, pathways may exist that do not continue into the direction toward the collecting electrode. Due to the macroscopic electric field over the active layer of the device carriers may be trapped inside those cul-de-sacs and cannot be collected. Therefore we also determined the fraction of ZnO connected to the top through a strictly rising path. The calculated unidirectionally connected fraction of ZnO is still very high (93%) for the 57 nm thin layer but reduces for thicker layers, reaching 80% for the 167 nm thick film.

Looking at the combined effects of charge carrier generation and collection we can conclude that the relative poor performance of thin P3HT:ZnO solar cells is related to inefficient charge generation as a result of the low ZnO content, the coarse phase separation, as well as the exciton losses impaired by the electrodes. For thicker photoactive layers charge generation is much more efficient, owing to a much more favourable phase separation. These device show superior efficiencies, but owing to increasing difficulty to collect the generated electrons the internal quantum efficiency maxes out at ca. 50%. Further improvement can be anticipated if better control over the morphology of the photoactive blend can be gained.

Methods

Substrates for device preparation were glass plates covered with patterned indium tin oxide (ITO). These substrates were thoroughly cleaned by sonication in acetone, and aqueous dodecyl sulphate solution, followed by rinsing with water and sonication in isopropanol and applying UV-ozone for 30 minutes. The substrates were then transferred to a nitrogen-filled glove box with a controlled humidity (RH) of 40%. PEDOT:PSS was applied by spin coating at 1500 rpm for one minute, and subsequent drying for 1 minute at 3000 rpm, followed by heating on a hot-plate at 100 ºC for 15 minutes. The active layer was deposited by spin coating the mixed solution of diethylzinc and P3HT.

Diethylzinc:P3HT solutions were prepared by mixing 350 μL of P3HT in chlorobenzene (14.3 mg mL^{-1}) with 150 μL of a diethylzinc solution (0.4 M, obtained by mixing 1.8 mL of a 1.1 M diethylzinc solution in toluene with 3.2 mL of THF). The final solution contained 10 mg mL^{-1} P3HT. Assuming full conversion of the diethylzinc to ZnO, this would afford a 1:1 (w/w) ratio of P3HT:ZnO in the mixed film.

Devices were all spin coated from the same solution at different spin speeds. The blends were aged for 15 min and then annealed for 15 min at 100 ºC in nitrogen. After heating the samples were transferred to a glove box with an inert nitrogen atmosphere (<1 ppm H_2O and <1 ppm O_2) using an air-tight container. The back electrode consisted of 100 nm of aluminium and was evaporated under high vacuum ($<3 \times 10^{-7}$ mbar). All handling and analysis of the cells was performed under inert atmosphere.

For TEM investigations, the P3HT:ZnO films were floated from the water soluble PEDOT:PSS substrate onto the surface of demineralised water and picked up with 200-mesh copper TEM grids. Bright-field TEM morphology observation and acquisition of tilt series for electron tomography were performed on a Technai G^2 20 TEM (FEI Co.) operated at 200 kV. All tilt series were obtained in an automatic fashion by using EXPLORE 3D software (FEI Co.), in the tilt range of ±70º with a saxton tilt scheme with a 0º tilt step of 1.5º. The alignment and (SIRT-)reconstruction of the data series was performed by using INSPEC 3D (FEI Co.) and visualization of the 3D reconstructed volume was done with Amira 4.1 (Mercury Computer Systems, Inc.). Cross-sectional specimen preparation from a complete device was performed by focused ion beam (FIB) machining applying a Quanta 3D FEG (FEI Co.).

For the statistical analysis and exciton diffusion modelling the electron tomography data were binarized. The threshold for this binarization has a major impact on the final outcome, and hence error margins were estimated by applying the two extremes for this threshold. N.B. these margins indicate the uncertainty within this particular sample. Larger differences can be expected between samples.

For the statistical analysis and exciton diffusion modelling only the homogeneous part of the morphology was used, leaving out the ill defined interfaces with PEDOT:PSS and aluminium. This part constitutes 60% of the total local P3HT:ZnO layer. In order to avoid overestimating edge effects in the diffusion modelling, the dataset is extended by mirroring part of the morphology until the correct thickness is obtained. The connectivity of the ZnO network was calculated for the reduced dataset and extrapolated to the correct thickness.

The diffusion equation is solved numerically by using a fully explicit scheme: $n(t + \Delta t) = n(t) + \Delta t\ (\mathrm{d}n/\mathrm{d}t)$, with the last term given by Equation 1. When steady-state is reached, i.e. when $\mathrm{d}n/\mathrm{d}t$ is smaller than a pre-set tolerance, the exciton density throughout the polymer phase is known. By comparing this with the exciton density in the absence of a quencher (τg), the quenching efficiency η_Q is obtained from $\eta_Q = 1- n/(\tau g)$.

References

1. Thompson, B. C. & Fréchet, J. M. J. Polymer-fullerene composite solar cells. *Angew. Chem. Int. Ed.* **47**, 58–77 (2008).
2. Park, S. H. *et al.* Bulk heterojunction solar cells with internal quantum efficiency approaching 100%. *Nat. Photonics* **3**, 297-303 (2009).
3. Liang, Y. *et al.* Highly efficient solar cell polymers developed via fine-tuning of structural and electronic properties. *J. the Am. Chem. Soc.* **131**, 7792-7799 (2009).
4. Huynh, W. U., Dittmer, J. J. & Alivisatos, A. P. Hybrid nanorod-polymer solar cells. *Science* **295**, 2425–2427 (2002).
5. Wang, P. *et al.* Photoinduced charge transfer and efficient solar energy conversion in a blend of a red polyfluorene copolymer with CdSe nanoparticles. *NanoLett.* **6**, 1789-1793 (2006).
6. Kwong, C. Y., Djurisic, A. B., Chui, P. C., Cheng, K. W. & Chan, W. K. Influence of solvent on film morphology and device performance of poly(3-hexylthiophene):TiO_2 nanocomposite solar cells. *Chem. Phys. Lett.* **384**, 372–375 (2004).
7. Kuo, C.Y., Tang, W.C., Gau, C., Guo, T. F. & Jeng, D. Z. Ordered bulk heterojunction solar cells with vertically aligned TiO_2 nanorods embedded in a conjugated polymer. *Appl. Phys. Lett.* **93**, 033307 (2008).
8. Beek, W. J. E., Wienk, M. M. & Janssen, R. A. J. Efficient hybrid solar cells from zinc oxide and a conjugated polymer. *Adv. Mater.* **16**, 1009–1013 (2004).

9. Beek, W. J. E., Wienk, M. M. & Janssen, R. A. J., Hybrid solar cells from regioregular polythiophene and ZnO nanoparticles. *Adv. Funct. Mater.* **16**, 1112–1116 (2006).
10. Olson, D. C., Shaheen, S. E., Collins, R. T. & Ginley, D. S. Effect of polymer processing on the performance of poly(3-hexylthiophene)/ZnO nanorod photovoltaic devices. *J. Phys. Chem. C* **111**, 16640–16645 (2007).
11. Wang, H. *et al.* Titania bicontinuous network structures for solar cell applications. *Appl. Phys. Lett.* **87**, 023507 (2005).
12. Ravirajan, P. *et al* Hybrid polymer/zinc oxide photovoltaic devices with vertically oriented ZnO nanorods and an amphiphilic molecular interface layer. *J. Phys. Chem. B* **110**, 7635–7639 (2006).
13. Zhu, R., Jiang, C.-Y. & Ramakrishna, S. Highly efficient nanoporous TiO_2-polythiophene hybrid solar cells based on interfacial modification using a metal-free organic dye. *Adv. Mater.* **21** 994–1000 (2009).
14. van Hal, P. A. *et al.* Photoinduced electron transfer and photovoltaic response of a MDMO-PPV:TiO_2 bulk-heterojunction. *Adv. Mater.* **15**, 118–121 (2003).
15. Beek, W. J. E., Slooff, L. H., Kroon, J. M., Wienk, M. M. & Janssen, R. A. J. Hybrid solar cells using a zinc oxide precursor and a conjugated polymer. *Adv. Funct. Mater.* **15**, 1703–1708 (2005).
16. Moet, D. J. D., Koster, L. J. A., de Boer, B. & Blom, P. W. M. Hybrid polymer solar cells from highly reactive diethylzinc: MDMO-PPV vs. P3HT. *Chem. Mater.* **19**. 5856–5861 (2007).

17. Schilinsky, P., Waldauf, C. & Brabec, C. J. Recombination and loss analysis in polythiophene based bulk heterojunction photodetectors. *Appl. Phys. Lett.***81**, 3885–3887 (2002).

18. van Hal, P. A., Christiaans, M. P. T., Wienk, M. M., Kroon, J. M. & Janssen, R. A. J. Photoinduced electron transfer from conjugated polymers to TiO_2. *J. Phys. Chem. B* **103**, 4352–4359 (1999).

19. Shim, M. & Guyot-Sionnest, P. Organic-capped ZnO nanocrystals: synthesis and n-type character. *J. Am. Chem. Soc.* **123**, 11651–11654 (2001).

20. Spano, F. C. Modeling disorder in polymer aggregates: The optical spectroscopy of regioregular poly(3-hexylthiophene) thin films, *J. Chem. Phys.* **122**, 234701 (2005).

21. Chang, J.-F. *et al*. Molecular-weight dependence of interchain polaron delocalization and exciton bandwidth in high-mobility conjugated polymers. *Phys. Rev. B.* **74**, 115318 (2006).

22. van Duren, J. K. J. *et al.* Relating the morphology of poly(*p*-phenylene vinylene)/methanofullerene blends to solar-cell performance, *Adv. Funct. Mater.* **14**. 425–434 (2004).

23. Yang, X., van Duren, J. K. J., Janssen, R. A. J., Michels, M. A. J. & Loos, J. Morphology and thermal stability of the active layer in poly(*p*-phenylenevinylene)/ methanofullerene plastic photovoltaic devices. *Macromolecules* **37**, 2151-2158 (2004).

24. Jinnai, H., Nishikawa, Y., Ikehara, T & Nishi, T. Emerging technologies for the 3D analysis of polymer structures *Adv. Polym. Sci.* **170**, 115–167 (2004).

25. Shaw, P. E., Ruseckas, A. & Samuel, I. D. W. Exciton diffusion measurements in poly(3-hexylthiophene). *Adv. Mater.* **20**, 3516–3520 (2008).
26. Piris, J. *et al.* The locus of free charge-carrier generation in solution-cast $Zn_{1-x}Mg_xO$/ poly(3-hexylthiophene) bilayers for photovoltaic applications. *Adv. Funct. Mater.* **17**, 3849–3857 (2007).
27. Becker, H., Burns, S. E. & Friend, R. H. Effect of metal films on the photoluminescence and electroluminescence of conjugated polymers. *Phys. Rev. B.* **56**, 1893–1905 (1997).
28. Yim, K.-H., Friend, R. H. & Kim, J. S. Anisotropic optical properties in electroluminescent conjugated polymers based on grazing angle photoluminescence measurements. *J. Chem. Phys.* **124**, 184706 (2006).
29. Markov, D. E. & Blom, P. W. M. Migration-assisted energy transfer at conjugated polymer/metal interfaces. *Phys. Rev. B.* **72**, 161401(R) (2005).

Acknowledgements

Authors gratefully acknowledge Dr. Dirk Veldman for assistance with the PIA measurements and Niek Lousberg for the preparing a cross-section of a complete device by focused ion beam (FIB). The research was supported by a TOP grant of the Chemical Sciences (CW) division of the Netherlands Organization for Scientific Research (NWO) and is part of the Joint Solar Programme (JSP). The JSP is co-financed by the Foundation for Fundamental Research on Matter (FOM), Chemical Sciences of NWO, and the Foundation Shell Research. This work was further supported by the Deutsche

Forschungsgemeinschaft under Priority Programme 1355 "Elementary Processes of Organic Photovoltaics", Senter/Novem in the EOS project Zomer (EOSLT03026), and is part of the research program of the Dutch Polymer Institute (DPI, project 524).

Author contributions

S.O. made and characterized the devices, S.v.B. did the TEM measurements. R.T. performed the statistical analysis. L.J.A.K. carried out the exciton diffusion calculations. J.G. did the optical modelling. M.W., J.L., V.S., and R.J. planned the research and supervised it. The article was written by S.O. and M.W.

Figure captions

Figure 1 | Performance of P3HT:ZnO solar cells.

a, Current density-voltage (*J*-*V*) characteristics of the best P3HT:ZnO device (film thickness is 225 nm) in the dark (black line) and under illumination with simulated solar light (red line). **b**, External quantum efficiency (EQE) of the same device, corrected for the non-linear response of the current with light intensity. Convolution of this spectral response with the AM1.5G solar spectrum provides an estimated current density of 5.6 mA cm^{-2}. The fraction of absorbed light, as calculated by optical modeling, using ellipsometry data is included. **c**, Evolution of the current density of P3HT:ZnO solar cells with the thickness of the active layer. For comparison, the amount of photons absorbed in the active layer is included. **d**, Internal quantum efficiency (IQE) of solar cells vs. thickness of the active layer. The scatter in the data is attributed to differences in the morphology for films of similar thickness, but manufactured independently.

Figure 2 | Photoinduced absorption spectra of P3HT:ZnO layers.

The normalized photoinduced absorption (PIA) spectra of P3HT:ZnO layers used in solar cells recorded at $T = 80$ K. In the devices the active layers had thicknesses of 44 nm (black), 54 nm (red), and 151 nm (blue). Spectra were normalized at the 2.2 eV bleaching band.

Figure 3. Electron tomography of P3HT:ZnO solar cells.

a, Transmission electron micrograph of a cross section of a typical P3HT:ZnO photovoltaic cell. The 80-100 nm thick sample was obtained using a focused ion beam

(FIB). The different layers present in the device are indicated in the image, the platinum layer is deposited later to allow preparation of the TEM sample. **b**, Reconstructed volumes of P3HT:ZnO layers, obtained by electron tomography. Three samples of 57 nm (left), 100 nm (centre), and 167 nm (right) are shown. The size of all samples is 800 × 800 nm; ZnO appears yellow, P3HT transparent. **c**, Reconstructed volume of a cross section of the active layer of a completed P3HT:ZnO device. **d**, The green arrow indicates an isolated ZnO domain. The red arrow indicates a ZnO domain that is connected to the top, but not through a strictly rising path.

Figure 4 | Statistical analysis of the 3D morphology.

a, Distribution of the probability to find a P3HT voxel at a certain distance from a ZnO domain for mixed P3HT:ZnO films of different thickness, calculated from the 3D-TEM data displayed in Fig. 3b. **b**, Cumulative probability to have P3HT within a shortest distance to ZnO. The error margins indicated are obtained from the two most extreme thresholds possible for the binarization of the 3D-TEM data.

Figure 5 | Exciton quenching efficiency cross sections in P3HT:ZnO bulk-heterojunctions.

a, **b**, **c**, Quenching efficiency in horizontal cross sections of bulk material of different thicknesses 57 nm (**a**), 100 nm (**b**) and 167 nm (**c**). The white areas constitute ZnO domains. **d**, **e**, **f**, Quenching efficiency in the vicinity of electrodes (gray areas) for different layer thicknesses 57 nm (**d**), 100 nm (**e**) and 167 nm (**f**).

Table 1 | Calculated volume fraction, exciton quenching and percolation connectivity of P3HT:ZnO bulk heterojunction layers inferred from electron tomography.

		Without electrodes	With electrodes			
Film thickness (nm)	ZnO volume fraction (%)	Quenched by ZnO (%)	Quenched by ZnO (%)	Quenched by electrodes (%)	ZnO connected to top (%)	ZnO monotonously connected to top (%)
57	13 ± 4	40 ± 3	32 ± 1	32 ± 1	96 ± 2	93 ± 2
100	21 ± 8	78 ± 5	73 ± 5	7 ± 1	94 ± 5	85 ± 10
167	21 ± 8	83 ± 5	79 ± 6	4 ± 1	92 ± 5	80 ± 12

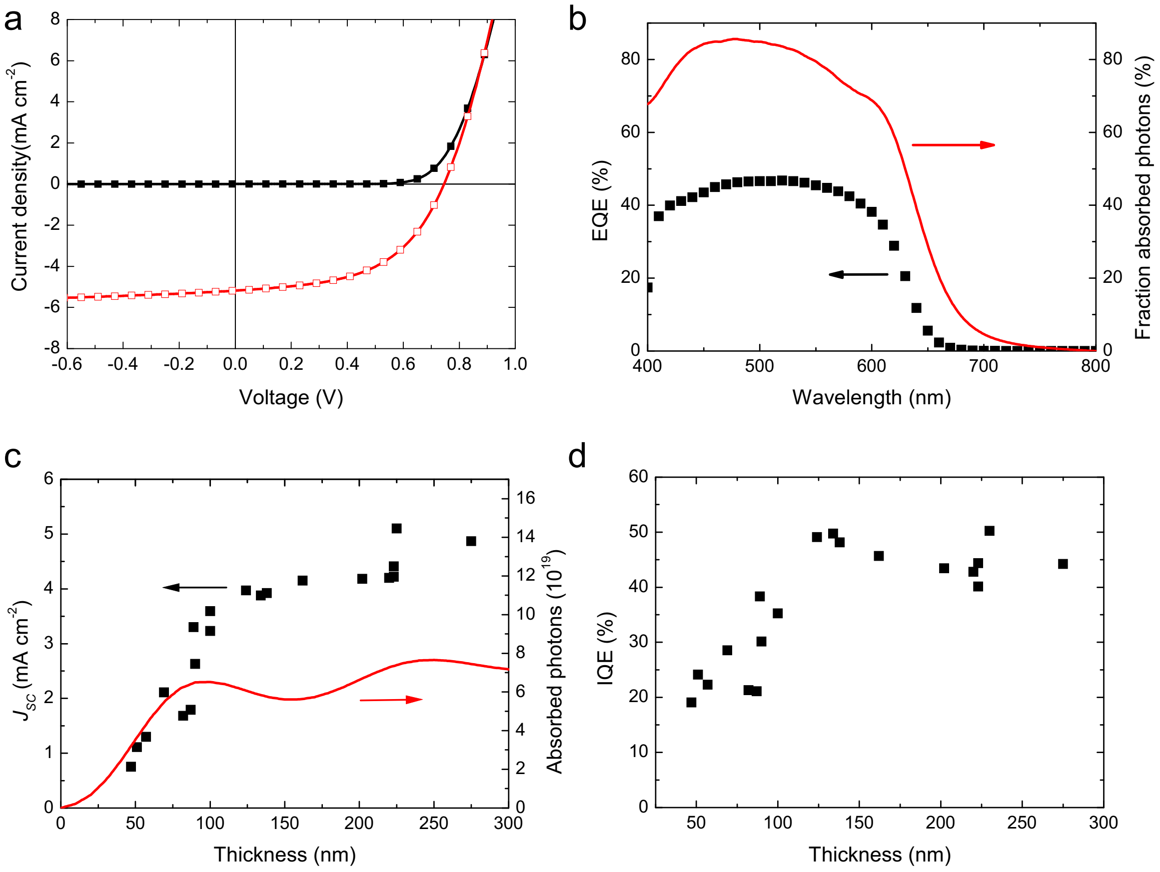
a
Current density(mA cm^{-2})
Voltage (V)
-0.6
-0.4
-0.2
0.0
0.2
0.4
0.6
0.8
1.0
8
6
4
2
0
-2
-4
-6
-8
b
EQE (%)
Fraction absorbed photons (%)
Wavelength (nm)
400
500
600
700
800
0
20
40
60
80
c
J_{SC} (mA cm^{-2})
Absorbed photons (10^{19})
Thickness (nm)
0
50
100
150
200
250
300
0
1
2
3
4
5
6
0
2
4
6
8
10
12
14
16
d
IQE (%)
Thickness (nm)
50
100
150
200
250
300
0
10
20
30
40
50
60

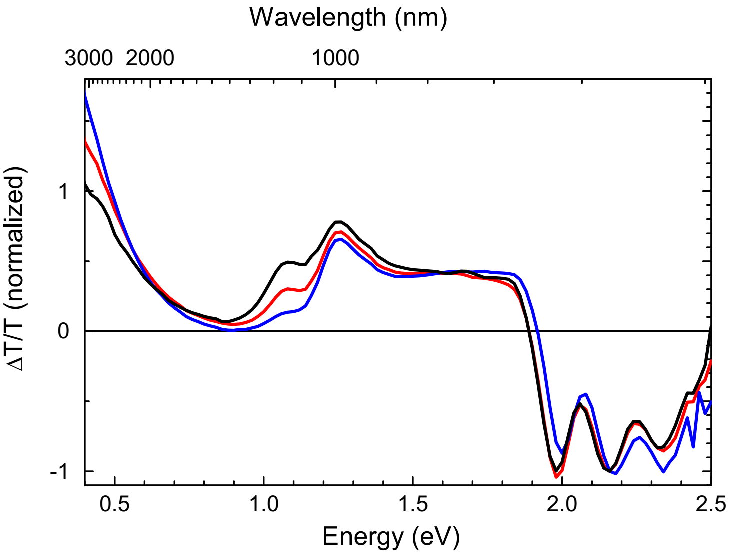
Wavelength (nm)
3000
2000
1000
ΔT/T (normalized)
1
0
-1
0.5
1.0
1.5
2.0
2.5
Energy (eV)

a

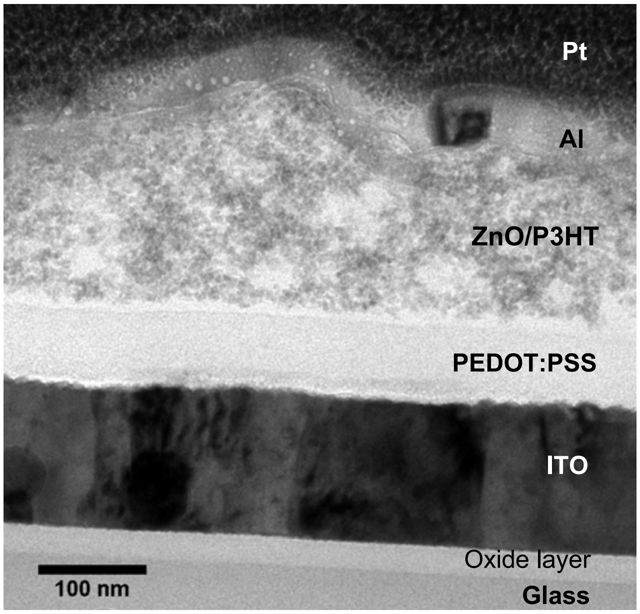
Pt
Al
ZnO/P3HT
PEDOT:PSS
ITO
Oxide layer
100 nm
Glass

b

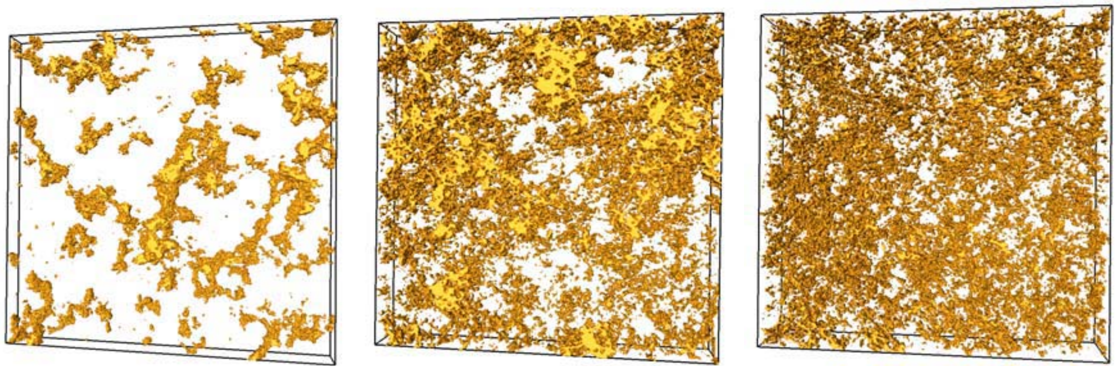

c

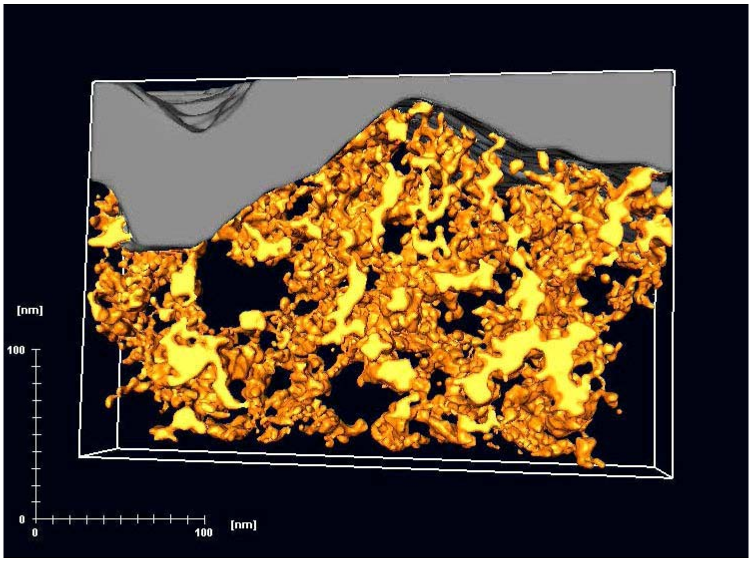
[nm]
100
0
0
100
[nm]

d

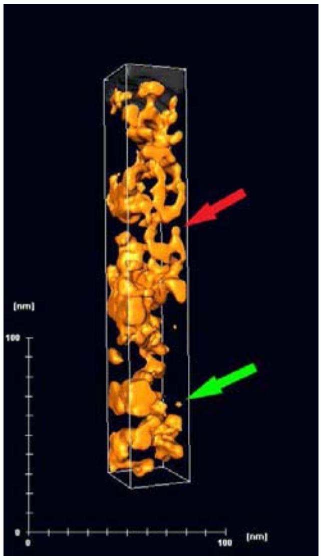
[nm]
100
0
0
100
[nm]

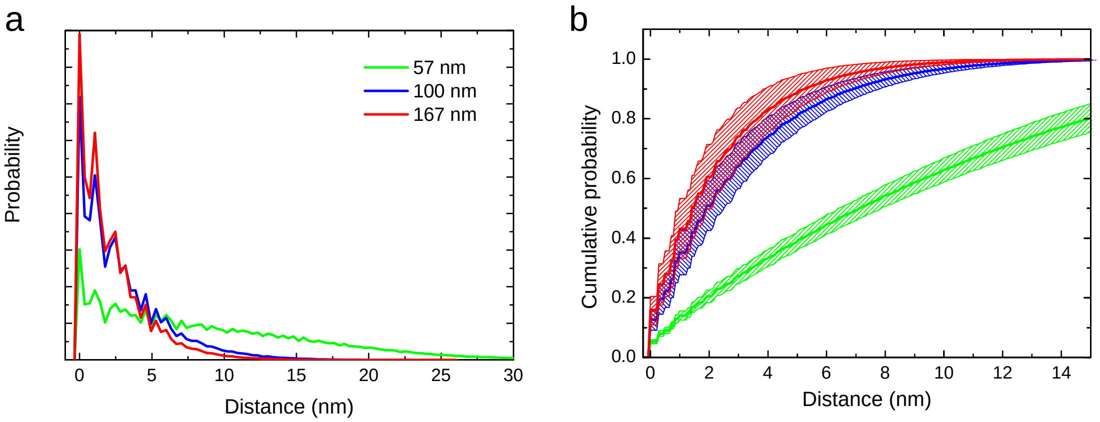
a
Probability
Distance (nm)
0
5
10
15
20
25
30
57 nm
100 nm
167 nm
b
Cumulative probability
Distance (nm)
0.0
0.2
0.4
0.6
0.8
1.0
0
2
4
6
8
10
12
14

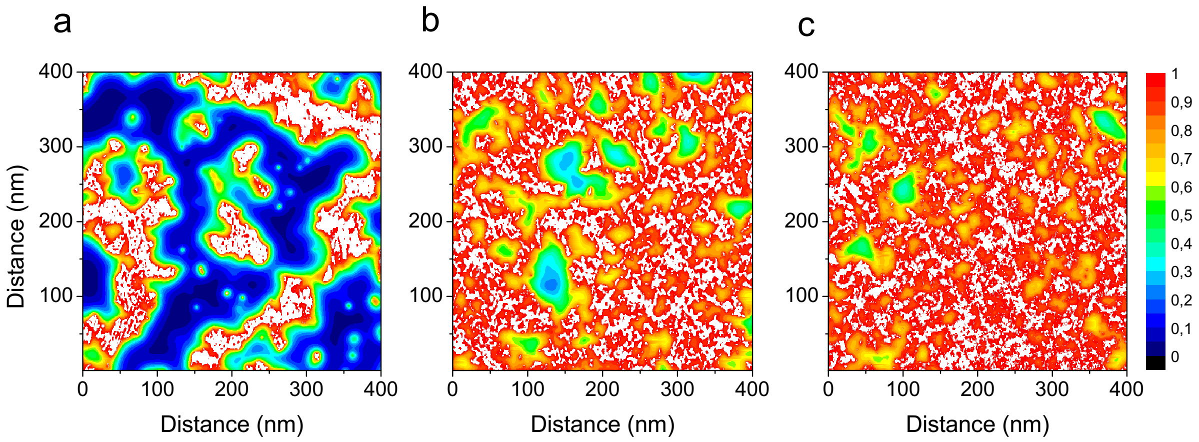
a
b
c
Distance (nm)
400
300
200
100
0
100
200
300
400
Distance (nm)
1
0,9
0,8
0,7
0,6
0,5
0,4
0,3
0,2
0,1
0

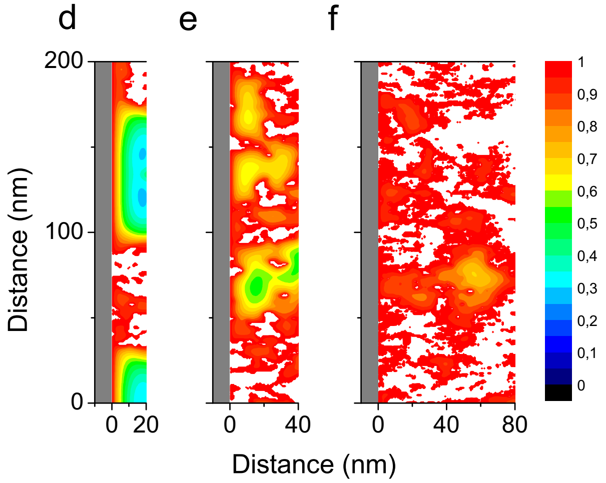
d
e
f
200
100
0
Distance (nm)
0
20
0
40
0
40
80
Distance (nm)
1
0,9
0,8
0,7
0,6
0,5
0,4
0,3
0,2
0,1
0